

HRRT Versus HR+ Human Brain PET Studies: An Interscanner Test–Retest Study

Floris H.P. van Velden, Reina W. Kloet, Bart N.M. van Berckel, Fred L. Buijs, Gert Luurtsema, Adriaan A. Lammertsma, and Ronald Boellaard

Department of Nuclear Medicine & PET Research, VU University medical center, Amsterdam, The Netherlands

The high-resolution research tomograph (HRRT) is a dedicated human brain PET scanner. The purpose of this study was to compare the quantitative accuracy of the HRRT with that of the clinical HR+ PET scanner and to assess effects of differences in spatial resolution between both scanners (~2.7 mm and ~7.0 mm for HRRT and HR+, respectively). **Methods:** Paired ^{11}C -flumazenil scans of 7 healthy volunteers were assessed. For each volunteer, dynamic scans (including arterial sampling) were acquired on both scanners on the same day, thereby minimizing intersubject variability. Volume of distribution was generated using Logan plot analysis with plasma input. In addition, other plasma input, reference tissue (with pons as the reference tissue input), and parametric methods were included in the interscanner comparison. **Results:** Logan volume-of-distribution analysis of HRRT data showed higher values than that of HR+ data (slope with the intercept fixed at the origin of 1.14 ± 0.10 to 1.19 ± 0.10 , depending on the HRRT reconstruction method used). Smoothing HRRT reconstructions with a 6-mm full width at half maximum gaussian kernel reduced this slope toward the line of identity (1.04 ± 0.11 to 1.07 ± 0.11), retaining good correlation between HR+ and HRRT data (r , ~0.98). Similar trends were observed for other plasma input, reference tissue, and parametric methods. However, after reference matching the reference tissue models showed lower HRRT kinetic parameter values than HR+ values (slope with fixed intercept, 0.90 ± 0.10 to 0.94 ± 0.13). **Conclusion:** Higher values of pharmacokinetic parameter values, obtained from HRRT versus HR+ PET studies, indicate improved HRRT PET quantification primarily due to a reduction in partial-volume effects.

Key Words: brain PET; high-resolution research tomograph; high spatial resolution

J Nucl Med 2009; 50:693–702

DOI: 10.2967/jnumed.108.058628

The availability of lutetium oxyorthosilicate/lutetium-yttrium oxyorthosilicate (LSO/LYSO) crystals has generated interest in new PET scanners that have higher spatial image resolution. The ECAT High-Resolution Research Tomograph (HRRT) (CTI/Siemens) is a dedicated human

brain scanner with design features that enable high spatial image resolution combined with high sensitivity (1). The HRRT is the first commercially available PET scanner that uses a double layer of LSO/LYSO crystals to achieve photon detection with depth-of-interaction information.

To date, only a limited number of human brain studies have been performed using the HRRT (2–7). Most human brain studies have been acquired with clinical (whole-body) PET scanners, such as the ECAT EXACT HR+ (CTI/Siemens). Therefore, it is worthwhile to compare the accuracy of quantitative human HRRT studies with that of HR+ studies. The HR+ scanner has a single layer of bismuth germinate crystals. Over the years, its quantitative accuracy has been studied extensively (8–10).

A direct quantitative comparison between HRRT and HR+ has been performed in a limited way, using only phantoms (11). Recently, Leroy et al. (3) performed a comparative study between similar patient groups, matched in age, acquired on either an HR+ or an HRRT. Although this study showed good agreement between studies performed on HRRT and HR+ scanners, results may have suffered from intersubject variability, as no paired scans in the same subjects were performed. Moreover, as suggested in the study of Leroy et al. (3), further studies for a variety of other PET tracers would be needed to fully validate the quantitative potential of the HRRT.

The purpose of the present study was to compare the quantitative accuracy of the HRRT scanner with that of the HR+ scanner and to assess the effects of differences in spatial resolution between both scanners. Paired ^{11}C -flumazenil brain scans in 7 healthy volunteers were assessed; that is, for each volunteer, images were acquired on both scanners on the same day, enabling a direct comparison between both PET scanners.

MATERIALS AND METHODS

Scanner Descriptions

The commercial HRRT, a dedicated high-resolution 3-dimensional (3D) human brain PET scanner, consists of 8 panel detectors (detector heads), which are arranged in an octagon (2). A detector head comprises 117 detector blocks, each cut into 8×8 crystal elements. Each block consists of 2 LSO/LYSO crystal layers to achieve photon detection with depth-of-interaction

Received Sep. 29, 2008; revision accepted Jan. 15, 2009.

For correspondence or reprints contact: Floris H.P. van Velden, Department of Nuclear Medicine & PET Research, VU University medical center, P.O. Box 7057, 1007MB, Amsterdam, The Netherlands. E-mail: f.vvelden@vumc.nl

COPYRIGHT © 2009 by the Society of Nuclear Medicine, Inc.

information. The spatial resolution is between 2.3- and 3.4-mm full width at half maximum (FWHM). The National Electrical Manufacturers Association NU 2-2001 sensitivity equals 39.8 kcps-kBq⁻¹·mL⁻¹ (12). The field of view measures 312 mm in diameter and 250 mm in the axial direction. For attenuation and scatter correction, transmission scans were acquired using a 740-MBq 2-dimensional (2D) fan-collimated ¹³⁷Cs (662 keV) moving point source (13). A detailed description of the scanner, its reconstruction software, and its performance has been reported previously (1).

The HR+ consists of 4 rings of 72 bismuth germinate block detectors, arranged in a circle, and each detector block (as for the HRRT) is cut into 8 × 8 elements. The axial field of view measures 155 mm, with a patient port of 562 mm. The spatial resolution is between 4.3- and 8.3-mm FWHM, depending on the position in the scanner. The National Electrical Manufacturers Association NU 2-2001 sensitivity equals 21.9 kcps-kBq⁻¹·mL⁻¹ (14). For attenuation and scatter correction, transmission scans were acquired using three 220-MBq ⁶⁸Ge rod (511 keV) sources. A detailed description of the scanner and its performance can be found elsewhere (9).

Test-Retest Study

Two 60-min dynamic scans (one on each scanner, in random order) were acquired for 7 healthy volunteers (age ± SD, 53 ± 16 y) immediately after administration of ¹¹C-flumazenil (365 ± 34 MBq) with a specific activity of 54 ± 24 GBq mL⁻¹. Administered doses and specific activities were not statistically significantly different between both scans (2-sided paired *t* test, *P* = 0.45 and *P* = 0.46, respectively). For the HRRT scanner, each emission scan was acquired in list mode and subsequently histogrammed into 16 time frames, with variable frame lengths (4 × 15, 4 × 60, 2 × 150, 2 × 300, and 4 × 600 s). For the HR+ scanner, emission scans were acquired in 3D mode and histogrammed online into 16 time frames according to the same scheme as for the HRRT. Before each emission scan (and tracer administration), a transmission scan was acquired for attenuation and scatter correction. In general, the attenuation-correction maps corresponded visually between the HR+ and the HRRT. However, as previously reported (15) the attenuation correction of the HRRT is reasonably accurate and corresponds well to that of the HR+. During the emission scan, continuous online arterial blood was sampled, using an automated blood-sampling device (16). At set times (5, 10, 15, 20, 30, 40, and 60 min after injection), continuous sampling was interrupted briefly to collect manual blood samples. After each sample was collected, the arterial line was flushed with heparinized sterile and isotonic saline. These manual sample data were used for calibrating the (online) blood sampler, measuring plasma and whole-blood ratios, and determining metabolite fractions (17,18). The fractions of metabolized and unchanged ¹¹C-flumazenil corresponded with a previous report (19), and deviations between metabolite fractions on the HR+ and HRRT scanners were not statistically different (2-sided paired *t* test, *P* > 0.1). The metabolite-corrected arterial plasma time-activity curve was used as the input function for analyzing kinetic data. A head-immobilization device was used to limit head movement. To ensure that head positions were the same during each scan and keep head motion to a minimum, several points were marked with ink on each subject's skin and the alignment of each point was checked with projected laser lines every 5–10 min. In addition to the PET scan, a structural T1-weighted MRI scan for each subject, used to define regions of

interest (ROIs), was acquired on a 1.5-T scanner (SONATA; Siemens Medical Solutions). The study was approved by the medical ethics committee of the VU University medical center, and all subjects gave written informed consent before scanning started.

Reconstructions

All reconstructed data were normalized and corrected for scatter, randoms, attenuation, decay, and dead time. For the HRRT scanner, all studies were reconstructed using both the newly implemented analytic 3D filtered backprojection (3D-FBP) algorithm, specifically customized and optimized for the HRRT (20), and the iterative 3D ordered-subsets weighted least-squares (3D-OSWLS) method, with 7 iterations and 16 subsets (21). 3D-FBP reconstructions are linear and therefore preferred for dynamic studies because these algorithms show no bias in frames with low noise-equivalent counts (NEC) (21–23). At present, this bias is still observed in some iteratively reconstructed HRRT images and depends on the methods and settings being used (11,21,23,24). However, as 3D-FBP reconstructions are noisier, 3D-OSWLS was also used in this study. 3D-OSWLS showed accuracy in patient studies similar to that of 3D-FBP (21) but resulted in a much lower pixel variance. For all HRRT reconstructions, randoms were estimated by the variance reduction on randoms algorithm (23,25). All HRRT-reconstructed images were also postsmoothed with a 6-mm FWHM gaussian kernel to match image resolution with that of the HR+ scanner.

For the HR+ scanner, 3D emission scans were rebinned using Fourier rebinning (FORE) and reconstructed using 2D-FBP. Again, 2D-FBP reconstructions are linear and are, therefore, preferred for quantitative dynamic PET studies (26).

Data Analysis

ROI Definition. ROIs were defined using gray-matter (GM) and white-matter (WM) segmentation of the coregistered structural MRI scan to derive GM and WM subregions of 15 different manually defined ROIs, namely the pons (used only as a reference region) and the left and right regions of the thalamus; frontal, temporal, parietal, and occipital lobes; caudate; and putamen (Supplemental Figure 1; supplemental materials are available online only at <http://jnm.snmjournals.org>). GM data were used for all regions except the pons, in which total (GM plus WM) data were used. MRI scans were coregistered using the software package VINCI (Max Planck Institute for Neurologic Research). In addition, the VINCI software was used to coregister the HR+ scan onto the HRRT scan, using the HRRT image matrix dimensions to minimize loss in resolution. In this way, exactly the same ROIs can be projected on both scans. GM and WM segmentation was performed using Statistical Parametric Mapping (SPM5; Wellcome Department of Cognitive Neurology, University College London). Other ROIs were drawn by hand using DISPLAY software (Montreal Neurologic Institute). ROIs were then projected either onto parametric images to derive regional pharmacokinetic parameters or onto reconstructed images to derive time-activity curves for the various regions, which subsequently were used for pharmacokinetic modeling.

Pharmacokinetic Parameter Analysis. Pharmacokinetic parameters were generated either from the various time-activity curves obtained using the ROI approach mentioned above or from parametric images generated using a parametric method. Parametric volume-of-distribution (V_T) images were generated using

Logan plot analysis with plasma input (27). In addition, V_T images were generated using a basis function method (BFM) of a single-tissue-compartment model (28). Furthermore, reference tissue parametric distribution volume ratio (DVR) images were generated using Logan plot analysis (RLogan) with the reference tissue input function (pons) (29), and parametric binding potential (BP_{ND}) images were generated with receptor parametric mapping (RPM), again with the pons as the reference tissue. RPM (30) is a basis-function implementation of the simplified reference tissue model (31). The same kinetic methods were used on various time-activity curves obtained using the ROI approach mentioned earlier. All parametric images and kinetic data from time-activity curves were generated using the software package PPET (32).

Quantitative Accuracy Assessment. HRRT-reconstructed images using various 3D reconstruction algorithms were compared with corresponding HR+ images reconstructed with 2D-FBP + FORE. From these images, regional and parametric pharmacokinetic parameters were derived and compared. The Pearson correlation coefficient (r), intercept (indicates possible bias), slope (indicates interscanner differences in quantification), slope with the intercept fixed at the origin, and r with the intercept fixed at the origin, calculated per subject, are reported as mean \pm SD. In addition, the standardized uptake value (SUV) was calculated as the measured activity concentration divided by injected activity divided by body weight of the subject.

Interscanner Test-Retest Study Overview

HR+ and HRRT scanners were compared. HRRT data were reconstructed using both 3D-FBP and 3D-OSWLS. For the HRRT scanner, data were used as without and with (6-mm FWHM gaussian kernel) resolution matching. HR+ data were reconstructed using FORE + 2D-FBP. All reconstructed data were analyzed using the following kinetic modeling methods (either based on time-activity curves or based on pixel-by-pixel [parametric] images): Logan V_T , BFM V_T , RLogan DVR, and RPM BP_{ND} . In addition, SUV curves, metabolite fractions, and subject motion were analyzed to provide quality control.

RESULTS

Outliers

One subject showed poor correspondence between HR+ and HRRT data in all analyses. One of this subject's carotid arteries was not visible on the HRRT scans, and this subject showed motion (at least 5 mm) on the HR+ scans. Therefore, this subject was excluded from comparisons. For another subject, no metabolite data were available and therefore no metabolite-corrected plasma input function could be generated. This subject was used only for comparison of data obtained with reference tissue models.

Plasma Input Models

Time-Activity Curve Analysis. Figure 1 shows the correlation between Logan-derived V_T obtained with various HRRT reconstruction methods and the corresponding Logan-derived V_T obtained with the HR+ for analyses based on time-activity curves. Table 1 shows mean Logan-derived V_T values and absolute variability for each brain region and illustrates that the application of resolution matching improves test-retest values. Figure 1 and Table 2 illustrate that smoothing HRRT reconstructions with a 6-mm FWHM gaussian kernel improved slopes (with the intercept fixed at the origin) from 1.19 ± 0.10 to 1.07 ± 0.11 (3D-FBP) and from 1.14 ± 0.10 to 1.04 ± 0.11 (3D-OSWLS), retaining a high correlation between HR+ and HRRT (r , ~ 0.98). Table 2 illustrates this effect for BFM-derived V_T , in which slopes with the intercept fixed at the origin improved from 1.29 ± 0.23 to 1.04 ± 0.22 (3D-FBP) and from 1.11 ± 0.22 to 1.00 ± 0.21 (3D-OSWLS), with r values between 0.88 ± 0.05 and 0.98 ± 0.01 .

Parametric Image Analysis. Correlation analyses of V_T obtained with HRRT and corresponding HR+ Logan-derived parametric images are shown in Table 3. Smoothing

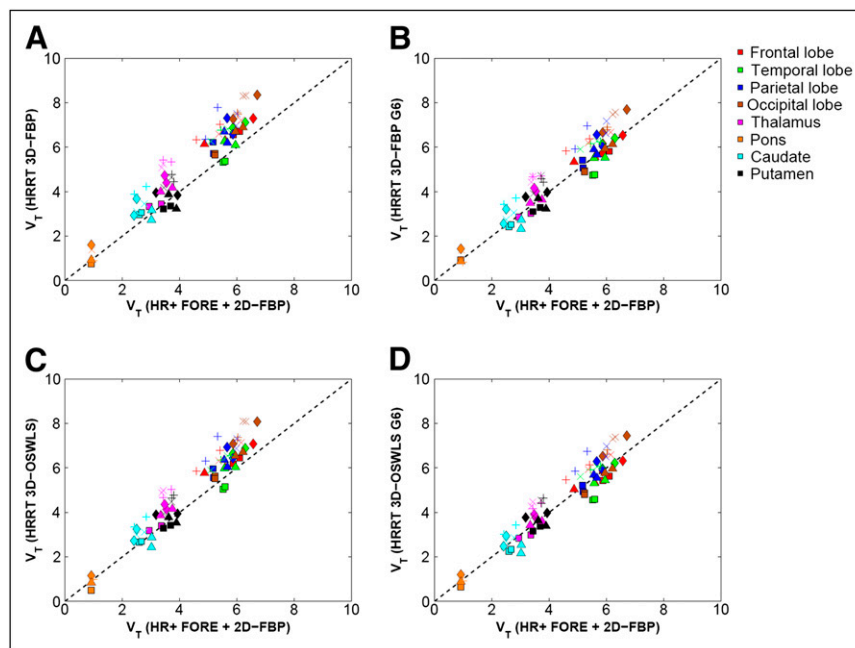


FIGURE 1. Correlation between Logan-derived V_T obtained with various HRRT reconstruction methods and corresponding Logan-derived V_T obtained with HR+ 2D-FBP + FORE: (A) 3D-FBP, (B) 3D-FBP G6, (C) 3D-OSWLS, and (D) 3D-OSWLS G6. Every symbol represents single subject; same symbol per subject represents different anatomic regions, each with different color (dashed line is line of identity). G6 = 6-mm FWHM gaussian kernel.

TABLE 1. Plasma Input and Reference Tissue Kinetic Data Using Time-Activity Curve Analysis

| ROI | Brain area | Side | Volume (mL) | Logan V_T | | | | RPM BP _{ND} | | | | |
|----------------|------------|------------|-------------|--------------|--------------------------|-----------------|--------------------------|-----------------------|------------------|--------------------------|------------------|--------------------------|
| | | | | HRRT (OSWLS) | | HRRT G6 (OSWLS) | | HRRT (OSWLS) | | HRRT G6 (OSWLS) | | |
| | | | | HR+, V_T | Absolute variability (%) | V_T | Absolute variability (%) | HR+, BP _{ND} | BP _{ND} | Absolute variability (%) | BP _{ND} | Absolute variability (%) |
| Frontal lobe | Left | 12.1 ± 2.6 | 5.3 ± 0.6 | 6.2 ± 0.4 | 15.0 ± 7.1 | 5.5 ± 0.4 | 7.8 ± 6.6 | 4.8 ± 0.9 | 5.4 ± 1.5 | 12.7 ± 8.6 | 4.6 ± 1.2 | 10.0 ± 10.8 |
| | Right | 14.8 ± 2.4 | 6.0 ± 0.5 | 6.7 ± 0.5 | 11.6 ± 7.2 | 6.0 ± 0.5 | 7.2 ± 3.5 | 5.4 ± 0.7 | 5.7 ± 1.2 | 10.6 ± 8.2 | 4.8 ± 1.0 | 13.3 ± 14.0 |
| Temporal lobe | Left | 22.5 ± 4.9 | 5.5 ± 0.3 | 6.0 ± 0.6 | 11.7 ± 3.6 | 5.5 ± 0.6 | 8.7 ± 6.5 | 5.0 ± 0.4 | 5.0 ± 0.8 | 9.1 ± 4.5 | 4.3 ± 0.5 | 15.3 ± 8.3 |
| | Right | 21.3 ± 5.8 | 5.9 ± 0.3 | 6.2 ± 0.7 | 9.0 ± 5.0 | 5.7 ± 0.7 | 8.1 ± 7.0 | 5.3 ± 0.4 | 5.0 ± 0.8 | 11.6 ± 6.0 | 4.4 ± 0.5 | 17.7 ± 10.1 |
| Parietal lobe | Left | 12.8 ± 3.4 | 5.5 ± 0.3 | 6.8 ± 0.6 | 20.1 ± 7.7 | 6.2 ± 0.7 | 10.4 ± 9.3 | 5.0 ± 0.4 | 5.8 ± 1.0 | 17.0 ± 11.5 | 5.0 ± 0.8 | 11.3 ± 8.2 |
| | Right | 12.6 ± 3.5 | 5.5 ± 0.5 | 6.2 ± 0.5 | 12.3 ± 7.6 | 5.7 ± 0.6 | 6.8 ± 6.6 | 4.9 ± 0.6 | 5.5 ± 1.4 | 15.4 ± 13.5 | 4.8 ± 1.0 | 13.6 ± 7.4 |
| Occipital lobe | Left | 18.7 ± 8.6 | 5.9 ± 0.4 | 6.9 ± 0.9 | 15.8 ± 7.2 | 6.2 ± 1.0 | 9.2 ± 4.7 | 5.2 ± 0.2 | 5.6 ± 0.8 | 13.4 ± 8.4 | 4.9 ± 0.5 | 11.1 ± 4.9 |
| | Right | 13.7 ± 4.5 | 6.1 ± 0.5 | 7.2 ± 1.1 | 15.6 ± 8.8 | 6.5 ± 1.1 | 10.3 ± 4.5 | 5.3 ± 0.7 | 5.8 ± 0.6 | 14.0 ± 11.9 | 4.9 ± 0.3 | 11.9 ± 5.6 |
| Thalamus | Left | 2.0 ± 0.9 | 3.3 ± 0.2 | 4.2 ± 0.7 | 21.1 ± 12.2 | 3.7 ± 0.6 | 11.6 ± 10.8 | 2.6 ± 0.3 | 3.3 ± 0.7 | 23.7 ± 13.7 | 2.8 ± 0.5 | 12.0 ± 8.0 |
| | Right | 2.3 ± 0.6 | 3.5 ± 0.2 | 4.4 ± 0.6 | 20.1 ± 14.3 | 3.8 ± 0.6 | 13.6 ± 7.3 | 2.8 ± 0.2 | 3.4 ± 0.4 | 18.1 ± 11.2 | 2.8 ± 0.3 | 8.1 ± 5.0 |
| Caudate | Left | 2.2 ± 0.3 | 2.6 ± 0.3 | 2.8 ± 0.3 | 19.8 ± 23.0 | 2.5 ± 0.3 | 19.1 ± 12.5 | 1.9 ± 0.5 | 2.1 ± 0.8 | 25.6 ± 6.0 | 1.7 ± 0.6 | 20.0 ± 23.0 |
| | Right | 2.1 ± 0.3 | 2.8 ± 0.2 | 3.1 ± 0.4 | 17.2 ± 10.9 | 2.8 ± 0.4 | 16.0 ± 12.0 | 2.0 ± 0.3 | 2.4 ± 0.4 | 17.4 ± 10.6 | 1.9 ± 0.3 | 10.4 ± 12.7 |
| Putamen | Left | 1.6 ± 0.9 | 3.7 ± 0.1 | 4.1 ± 0.5 | 14.6 ± 12.5 | 4.0 ± 0.6 | 13.9 ± 6.2 | 3.1 ± 0.3 | 3.2 ± 0.7 | 11.4 ± 9.6 | 3.0 ± 0.5 | 7.6 ± 12.0 |
| | Right | 1.9 ± 0.7 | 3.5 ± 0.3 | 3.9 ± 0.5 | 10.7 ± 9.6 | 3.7 ± 0.5 | 10.2 ± 9.7 | 2.9 ± 0.6 | 3.1 ± 0.7 | 9.0 ± 7.5 | 2.8 ± 0.6 | 9.9 ± 9.8 |
| Pons | — | 5.5 ± 0.6 | 0.9 ± 0.0 | 0.9 ± 0.2 | 13.7 ± 7.3 | 1.0 ± 0.2 | 13.3 ± 3.8 | — | — | — | — | — |

G6 = 6-mm FWHM gaussian kernel.

Logan V_T , RPM BP_{ND}, and absolute-variability values (mean ± SD for all values) using HRRT- vs. HR+-reconstructed scans of 5 subjects for various ROIs. Absolute variability (test-retest) is calculated as $|HRRT - HR+| / ((HRRT + HR+) \cdot 0.5) \cdot 100\%$.

TABLE 2. Plasma Input Kinetic Data Using Time–Activity Curve Analysis

| Pharmacokinetic parameter | HRRT reconstruction method | Unfixed intercept | | | Fixed intercept to origin | |
|---------------------------|----------------------------|-------------------|--------------|-------------|---------------------------|-------------|
| | | Slope | Intercept | <i>r</i> | Slope | <i>r</i> |
| Logan V_T | 3D-FBP | 1.15 ± 0.05 | 0.19 ± 0.43 | 0.97 ± 0.01 | 1.19 ± 0.10 | 0.97 ± 0.01 |
| | 3D-FBP G6 | 1.03 ± 0.07 | 0.20 ± 0.34 | 0.98 ± 0.00 | 1.07 ± 0.11 | 0.98 ± 0.01 |
| | 3D-OSWLS | 1.15 ± 0.05 | −0.03 ± 0.32 | 0.98 ± 0.00 | 1.14 ± 0.10 | 0.98 ± 0.00 |
| | 3D-OSWLS G6 | 1.02 ± 0.07 | 0.09 ± 0.27 | 0.98 ± 0.00 | 1.04 ± 0.11 | 0.98 ± 0.00 |
| BFM V_T | 3D-FBP | 0.99 ± 0.21 | 1.21 ± 0.35 | 0.93 ± 0.03 | 1.29 ± 0.23 | 0.88 ± 0.05 |
| | 3D-FBP G6 | 1.08 ± 0.17 | −0.16 ± 0.32 | 0.98 ± 0.01 | 1.04 ± 0.22 | 0.98 ± 0.01 |
| | 3D-OSWLS | 1.14 ± 0.17 | −0.13 ± 0.45 | 0.98 ± 0.01 | 1.11 ± 0.22 | 0.97 ± 0.00 |
| | 3D-OSWLS G6 | 1.08 ± 0.18 | −0.28 ± 0.28 | 0.98 ± 0.00 | 1.00 ± 0.21 | 0.98 ± 0.00 |

G6 = 6-mm FWHM gaussian kernel.
Slope, intercept, and *r* (all data are mean ± SD) of plasma input kinetic data using HRRT- vs. HR+-reconstructed scans of 5 subjects, over various ROIs.

HRRT data to approximate HR+ resolution improved the *r* from 0.91 ± 0.08 to 0.98 ± 0.01 (3D-FBP) and from 0.97 ± 0.01 to 0.98 ± 0.00 (3D-OSWLS). For parametric data, the slope with fixed intercept changed from 0.99 ± 0.12 to 1.07 ± 0.11 for 3D-FBP and from 1.07 ± 0.11 to 1.01 ± 0.10 for 3D-OSWLS when smoothing was applied. For BFM-derived V_T , correlations improved in a way similar to those obtained with analyses based on time–activity curves. For 3D-FBP, the slope with the intercept fixed at the origin changed from 1.29 ± 0.20 to 1.09 ± 0.15, and *r* improved from 0.89 ± 0.12 to 0.98 ± 0.01. For 3D-OSWLS, a change from 1.16 ± 0.14 to 1.00 ± 0.10 was observed (*r*, ~0.97).

Reference Tissue Models

In Figure 2, correlations are shown for time–activity curve–based, RLogan-derived DVR between various HRRT reconstructions and the corresponding HR+ data. One subject (indicated by the symbol × in Fig. 2) showed poor performance for all reference tissue methods (using analyses based either on time–activity curves or on parametric images), and another subject (indicated by symbol ○ in

Fig. 2) showed poor correspondence between HRRT 3D-FBP only (again for analyses based either on time–activity curves or on parametric images). These outliers resulted in high SD on slopes with a fixed intercept (0.18–0.54, Table 4), especially for 3D-FBP (0.37–0.54). The same trends were observed for RPM-derived BP_{ND} (Table 4) and for all results from the comparison of parametric reference tissue data (Table 5). However, trends similar to those observed in Tables 4 and 5 were observed for plasma input models (Tables 2 and 3), in which significant reductions in slopes with the intercept fixed at the origin were found by smoothing HRRT reconstructions with a 6-mm FWHM gaussian kernel (*P* < 0.05, 2-sided paired *t* test).

SUV Curve Analysis. Figure 3 shows SUV curves of a typical subject with a standard dose (382 ± 28 MBq), subject × (with lower SUV and a lower dose of about 311 ± 13 MBq), and subject ○ (with a lower HRRT dose of 305 MBq) for reference tissue (pons) and a typical cortical region (temporal lobe). The first (typical) subject showed hardly any differences between HR+- and HRRT-reconstructed SUVs. Similar results were found for 3 other subjects; for another 2 subjects, the pons SUV curves deviated either

TABLE 3. Plasma Input Parametric Image Data

| Pharmacokinetic parameter | HRRT reconstruction method | Unfixed intercept | | | Fixed intercept to origin | |
|---------------------------|----------------------------|-------------------|-------------|-------------|---------------------------|-------------|
| | | Slope | Intercept | <i>r</i> | Slope | <i>r</i> |
| Logan V_T | 3D-FBP | 0.83 ± 0.13 | 0.78 ± 0.54 | 0.94 ± 0.03 | 0.99 ± 0.12 | 0.91 ± 0.08 |
| | 3D-FBP G6 | 1.03 ± 0.05 | 0.21 ± 0.40 | 0.98 ± 0.00 | 1.07 ± 0.11 | 0.98 ± 0.01 |
| | 3D-OSWLS | 1.04 ± 0.07 | 0.17 ± 0.38 | 0.97 ± 0.01 | 1.07 ± 0.11 | 0.97 ± 0.01 |
| | 3D-OSWLS G6 | 0.98 ± 0.06 | 0.15 ± 0.30 | 0.99 ± 0.00 | 1.01 ± 0.10 | 0.98 ± 0.00 |
| BFM V_T | 3D-FBP | 1.00 ± 0.14 | 1.44 ± 0.80 | 0.96 ± 0.01 | 1.29 ± 0.20 | 0.89 ± 0.12 |
| | 3D-FBP G6 | 1.05 ± 0.11 | 0.18 ± 0.41 | 0.98 ± 0.01 | 1.09 ± 0.15 | 0.98 ± 0.01 |
| | 3D-OSWLS | 1.10 ± 0.12 | 0.29 ± 0.41 | 0.97 ± 0.01 | 1.16 ± 0.14 | 0.97 ± 0.01 |
| | 3D-OSWLS G6 | 0.98 ± 0.06 | 0.11 ± 0.32 | 0.98 ± 0.00 | 1.00 ± 0.10 | 0.98 ± 0.00 |

G6 = 6-mm FWHM gaussian kernel.
Slope, intercept, and *r* (all data are mean ± SD) of plasma input kinetic data using HRRT- vs. HR+-reconstructed scans of 5 subjects, over various ROIs.

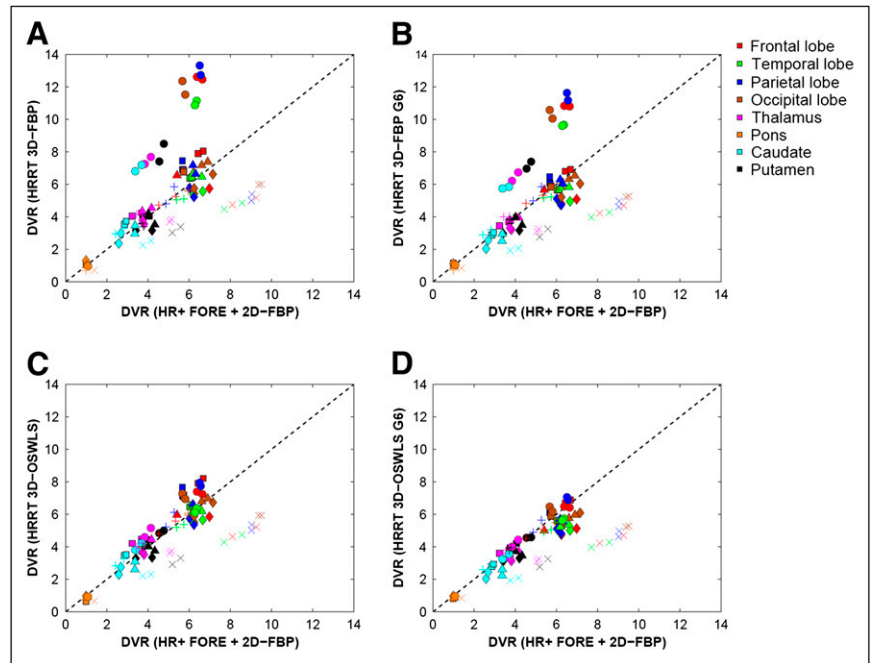


FIGURE 2. Correlation between RLogan-derived DVR obtained with various HRRT reconstruction methods and corresponding RLogan-derived DVR obtained with HR+ 2D-FBP + FORE: (A) 3D-FBP, (B) 3D-FBP G6, (C) 3D-OSWLS, and (D) 3D-OSWLS G6. Every symbol represents single subject; same symbol per subject represents different anatomic regions, each with different color (dashed line is line of identity). G6 = 6-mm FWHM gaussian kernel.

for HRRT 3D-FBP (subject ○) or for both HRRT 3D-FBP and 3D-OSWLS (subject ×).

Time-Activity Curve Analysis. After the outliers were removed (subject × for HR+ versus HRRT 3D-OSWLS and subjects × and ○ for HR+ versus HRRT 3D-FBP), reductions in slope with the intercept fixed at the origin were found for RLogan-derived DVR from time-activity curves (Table 6) by smoothing HRRT reconstructions with a 6-mm FWHM gaussian kernel, again retaining a lower SD on slopes with fixed intercept (0.10–0.15). Slopes with the intercept fixed at the origin lowered from 1.03 ± 0.12 to 0.94 ± 0.10 (3D-FBP) and from 1.04 ± 0.13 to 0.92 ± 0.10 (3D-OSWLS), with an r of 0.93 ± 0.02 to 0.96 ± 0.01 . This effect was also observed for RPM-derived BP_{ND} , in which slopes with the intercept fixed at the origin

decreased from 1.04 ± 0.14 to 0.92 ± 0.11 (3D-FBP) and from 1.04 ± 0.14 to 0.90 ± 0.10 (3D-OSWLS), with an r of 0.91 ± 0.10 to 0.96 ± 0.01 . Table 1 also shows mean RPM-derived BP_{ND} values and absolute variability for each brain region. This table illustrates that, by applying resolution matching, test-retest values in general improve, except for in regions close to the skull (i.e., temporal and frontal lobes).

Parametric Image Analysis. Table 7 shows RLogan data (excluding the outliers mentioned above) similar to those in Table 6, but with parametric data. Smoothing the HRRT data to approximate the HR+ resolution provided a good SD on slopes with a fixed intercept of 0.07–0.11. Slopes with the intercept fixed at the origin, however, were lower than those with analyses based on time-activity curves

TABLE 4. Reference Tissue Kinetic Data Using Time-Activity Curve Analysis (with Outliers)

| Pharmacokinetic parameter | HRRT reconstruction method | Unfixed intercept | | | Fixed intercept to origin | |
|---------------------------|----------------------------|-------------------|------------------|-----------------|---------------------------|-----------------|
| | | Slope | Intercept | r | Slope | r |
| RLogan DVR | 3D-FBP | 1.10 ± 0.51 | 0.02 ± 0.51 | 0.97 ± 0.01 | 1.10 ± 0.44 | 0.97 ± 0.01 |
| | 3D-FBP G6 | 0.99 ± 0.43 | 0.06 ± 0.44 | 0.98 ± 0.00 | 1.00 ± 0.37 | 0.98 ± 0.01 |
| | 3D-OSWLS | 0.98 ± 0.24 | 0.01 ± 0.27 | 0.98 ± 0.01 | 0.98 ± 0.22 | 0.98 ± 0.01 |
| | 3D-OSWLS G6 | 0.85 ± 0.20 | 0.10 ± 0.21 | 0.98 ± 0.00 | 0.87 ± 0.18 | 0.98 ± 0.00 |
| RPM BP_{ND} | 3D-FBP | 1.11 ± 0.56 | 0.11 ± 0.23 | 0.97 ± 0.01 | 1.14 ± 0.54 | 0.97 ± 0.01 |
| | 3D-FBP G6 | 0.96 ± 0.45 | 0.16 ± 0.38 | 0.97 ± 0.02 | 1.00 ± 0.44 | 0.96 ± 0.05 |
| | 3D-OSWLS | 1.00 ± 0.25 | -0.05 ± 0.46 | 0.98 ± 0.01 | 0.99 ± 0.25 | 0.97 ± 0.01 |
| | 3D-OSWLS G6 | 0.86 ± 0.20 | -0.05 ± 0.29 | 0.98 ± 0.00 | 0.85 ± 0.20 | 0.98 ± 0.01 |

G6 = 6-mm FWHM gaussian kernel.

Slope, intercept, and r (all data are mean \pm SD) of reference tissue (pons) kinetic data using HRRT- vs. HR+-reconstructed scans of 6 subjects, over various ROIs.

TABLE 5. Reference Tissue Parametric Image Data (with Outliers)

| Pharmacokinetic parameter | HRRT reconstruction method | Unfixed intercept | | | Fixed intercept to origin | |
|---------------------------|----------------------------|-------------------|-------------|-------------|---------------------------|-------------|
| | | Slope | Intercept | <i>r</i> | Slope | <i>r</i> |
| RLogan DVR | 3D-FBP | 0.74 ± 0.25 | 0.94 ± 0.40 | 0.94 ± 0.02 | 0.93 ± 0.27 | 0.88 ± 0.11 |
| | 3D-FBP G6 | 0.97 ± 0.41 | 0.10 ± 0.46 | 0.98 ± 0.00 | 0.99 ± 0.34 | 0.98 ± 0.01 |
| | 3D-OSWLS | 1.04 ± 0.07 | 0.17 ± 0.38 | 0.97 ± 0.01 | 1.07 ± 0.11 | 0.97 ± 0.01 |
| | 3D-OSWLS G6 | 0.87 ± 0.18 | 0.18 ± 0.27 | 0.98 ± 0.00 | 0.91 ± 0.16 | 0.98 ± 0.00 |
| RPM BP _{ND} | 3D-FBP | 0.89 ± 0.35 | 0.94 ± 0.44 | 0.97 ± 0.01 | 1.10 ± 0.43 | 0.92 ± 0.07 |
| | 3D-FBP G6 | 0.97 ± 0.38 | 0.10 ± 0.26 | 0.98 ± 0.00 | 1.00 ± 0.40 | 0.98 ± 0.01 |
| | 3D-OSWLS | 1.10 ± 0.12 | 0.29 ± 0.41 | 0.97 ± 0.01 | 1.16 ± 0.14 | 0.97 ± 0.01 |
| | 3D-OSWLS G6 | 0.91 ± 0.23 | 0.02 ± 0.22 | 0.98 ± 0.00 | 0.91 ± 0.20 | 0.98 ± 0.00 |

G6 = 6-mm FWHM gaussian kernel.

Slope, intercept, and *r* (all data are mean ± SD) of reference tissue (pons) kinetic data using HRRT- vs. HR+-reconstructed scans of 6 subjects, over various ROIs.

(parametric slopes changed from 0.89 ± 0.07 to 0.94 ± 0.10 for 3D-FBP and from 1.01 ± 0.11 to 0.93 ± 0.11 for 3D-OSWLS). For RPM-derived BP_{ND}, slopes and correlation always showed reduction (improvement) in slope. Slopes with the intercept fixed at the origin decreased from 1.04 ± 0.14 to 0.94 ± 0.13 , with an *r* of 0.83 ± 0.15 to 0.96 ± 0.01 (3D-FBP), and from 1.08 ± 0.19 to 0.93 ± 0.15 , with an *r* of 0.94 ± 0.03 to 0.97 ± 0.01 (3D-OSWLS).

DISCUSSION

Plasma Input Models

Smoothing HRRT-reconstructed images to obtain approximately the same resolution as that of the HR+ images resulted in quantitatively similar kinetic parameter values for both scanners, when using ROI-derived time–activity curve and plasma input (Fig. 1; Table 2), and an improvement in test–retest values (Table 1). This result is consistent with a previous phantom study (11) and a study by Leroy et al. (3).

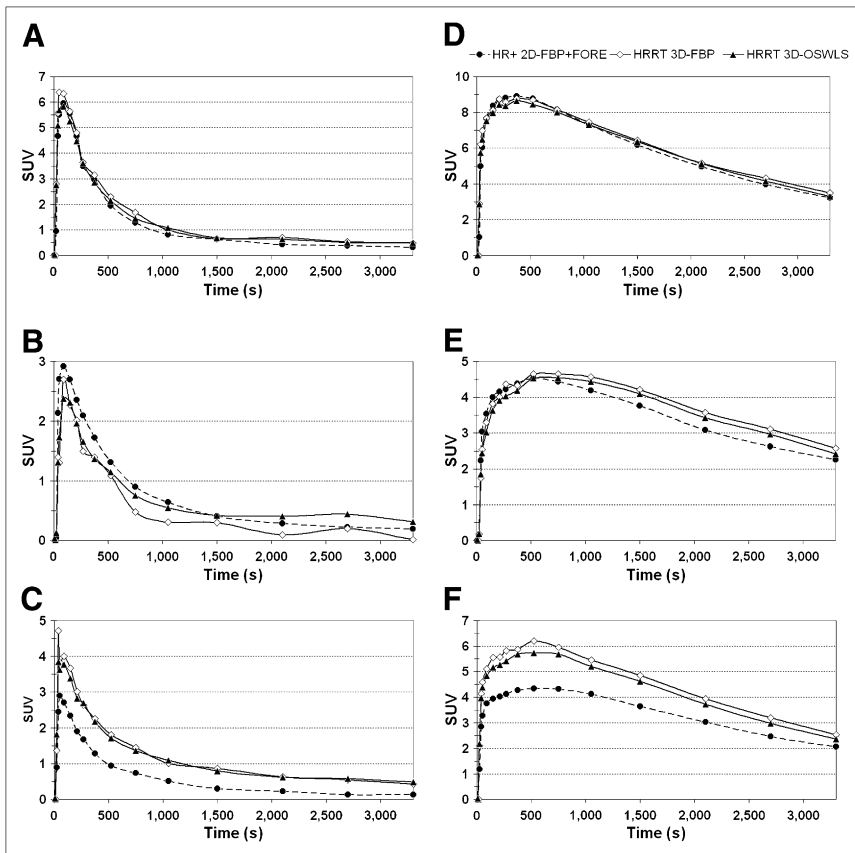


FIGURE 3. Reconstructed pons (A–C) and temporal lobe (D–F) SUV curves for HR+ and HRRT reconstruction methods for typical subject with a high dose (382 ± 28 MBq) (A, D), subject ○ with a low SUV and a low dose for HRRT (305 MBq) (B, E), and subject × with a low dose in general (311 ± 13 MBq) (C, F).

TABLE 6. Reference Tissue Kinetic Data Using Time–Activity Curve Analysis (Without Outliers)

| Pharmacokinetic parameter | HRRT reconstruction method | Unfixed intercept | | | Fixed intercept to origin | |
|---------------------------|----------------------------|-------------------|--------------|-------------|---------------------------|-------------|
| | | Slope | Intercept | <i>r</i> | Slope | <i>r</i> |
| | | RLogan DVR | 3D-FBP | 0.99 ± 0.18 | 0.17 ± 0.40 | 0.97 ± 0.01 |
| | 3D-FBP G6 | 0.91 ± 0.13 | 0.18 ± 0.32 | 0.98 ± 0.01 | 0.94 ± 0.10 | 0.95 ± 0.01 |
| | 3D-OSWLS | 1.03 ± 0.17 | 0.00 ± 0.34 | 0.98 ± 0.00 | 1.04 ± 0.13 | 0.96 ± 0.01 |
| | 3D-OSWLS G6 | 0.89 ± 0.12 | 0.12 ± 0.24 | 0.98 ± 0.00 | 0.92 ± 0.10 | 0.96 ± 0.01 |
| RPM BP _{ND} | 3D-FBP | 0.99 ± 0.17 | 0.22 ± 0.20 | 0.97 ± 0.01 | 1.04 ± 0.14 | 0.94 ± 0.03 |
| | 3D-FBP G6 | 0.86 ± 0.18 | 0.27 ± 0.42 | 0.97 ± 0.03 | 0.92 ± 0.11 | 0.91 ± 0.10 |
| | 3D-OSWLS | 1.05 ± 0.21 | −0.05 ± 0.57 | 0.98 ± 0.01 | 1.04 ± 0.15 | 0.95 ± 0.02 |
| | 3D-OSWLS G6 | 0.89 ± 0.12 | 0.00 ± 0.36 | 0.98 ± 0.00 | 0.90 ± 0.10 | 0.96 ± 0.01 |

G6 = 6-mm FWHM gaussian kernel.

Slope, intercept, and *r* (all data are mean ± SD) of reference tissue (pons) kinetic data using HRRT- vs. HR+-reconstructed scans of 4 subjects for 3D-FBP and 5 subjects for 3D-OSWLS, over various ROIs.

In the latter study, it was shown that the HRRT scanner, compared with the HR+ scanner, allowed for the recovery of higher kinetic parameter values (reference tissue BP_{ND} values) in the case of ¹¹C-PE2I nortropane and an age-matched population. As suggested in that study, however, further studies for a variety of PET tracers would be needed to fully validate the quantitative potential of the HRRT. In the present study, an attempt was made to minimize intersubject variability by acquiring paired scans (i.e., using both the HR+ and the HRRT) in the same subjects. This study further substantiates the findings of Leroy et al. (3), validating the HRRT for a different radiotracer using a different tracer kinetic plasma input model.

When using parametric image data, Logan V_T values obtained with the HRRT were lower than those obtained with the HR+ (Table 3). This was due to noise-induced bias when using the graphical Logan V_T method (33). BFM does not suffer from noise-induced bias and, therefore, showed the same V_T pattern for both ROI and parametric data.

The data presented in Table 1 showed poorer absolute-variability values than did data described in a previous

report (19) (6.8%–19.1% instead of 4.6%–8.4%). This might be caused by the smaller population used in this study.

Consistent with the study of Leroy et al. (3), the present study illustrates that, on the basis of the higher resolution, higher kinetic parameter values can be obtained with the HRRT. Because these differences disappear after resolution matching, they are primarily a result of different partial-volume effects.

Reference Tissue Models

The data presented in Table 1 showed only slightly poorer absolute-variability values than did data in a previous report (19) (7.6%–20.0% instead of 6.5%–17.0%). One subject (subject ○) with a low administered HRRT dose (305 MBq, Fig. 3B) showed a noisier pons time–activity curve for 3D-FBP than for 3D-OSWLS. This subject appeared to be an outlier for all HRRT 3D-FBP–related kinetic reference tissue analyses (Figs. 2A and 2B), with substantially higher parameter values than for the corresponding HR+ data, especially after resolution matching. For example, RLogan DVR values for this particular

TABLE 7. Reference Tissue Parametric Image Data (Without Outliers)

| Pharmacokinetic parameter | HRRT reconstruction method | Unfixed intercept | | | Fixed intercept to origin | |
|---------------------------|----------------------------|-------------------|-------------|-------------|---------------------------|-------------|
| | | Slope | Intercept | <i>r</i> | Slope | <i>r</i> |
| | | RLogan DVR | 3D-FBP | 0.71 ± 0.15 | 0.90 ± 0.48 | 0.94 ± 0.02 |
| | 3D-FBP G6 | 0.90 ± 0.13 | 0.20 ± 0.39 | 0.98 ± 0.01 | 0.94 ± 0.10 | 0.95 ± 0.02 |
| | 3D-OSWLS | 0.96 ± 0.15 | 0.23 ± 0.38 | 0.97 ± 0.01 | 1.01 ± 0.11 | 0.93 ± 0.04 |
| | 3D-OSWLS G6 | 0.90 ± 0.13 | 0.17 ± 0.29 | 0.98 ± 0.00 | 0.93 ± 0.11 | 0.96 ± 0.01 |
| RPM BP _{ND} | 3D-FBP | 0.84 ± 0.18 | 0.85 ± 0.35 | 0.97 ± 0.01 | 1.04 ± 0.14 | 0.83 ± 0.15 |
| | 3D-FBP G6 | 0.92 ± 0.14 | 0.09 ± 0.28 | 0.98 ± 0.00 | 0.94 ± 0.13 | 0.96 ± 0.01 |
| | 3D-OSWLS | 1.01 ± 0.23 | 0.29 ± 0.28 | 0.98 ± 0.01 | 1.08 ± 0.19 | 0.94 ± 0.03 |
| | 3D-OSWLS G6 | 0.92 ± 0.19 | 0.04 ± 0.25 | 0.98 ± 0.00 | 0.93 ± 0.15 | 0.97 ± 0.01 |

G6 = 6-mm FWHM gaussian kernel.

Slope, intercept, and *r* (all data are mean ± SD) of reference tissue (pons) kinetic data using HRRT- vs. HR+-reconstructed scans of 4 subjects for 3D-FBP and 5 subjects for 3D-OSWLS, over various ROIs.

subject, when compared with average RLogan DVR values for the other 4 subjects, were higher for HRRT 3D-FBP (4.6 ± 1.6 vs. 4.0 ± 1.4 , respectively). This effect is likely explained by the lower SUV (2.7 ± 0.3 in pons time-activity curve peak) for all reconstructions and all scanners for that 1 subject than that for the other subjects (4.2 ± 1.3 in pons time-activity curve peak). Iterative HRRT 3D-OSWLS, which is less sensitive to noise, provided better correspondence between HR+ and HRRT data than did HRRT 3D-FBP, indicating that noise may affect reference tissue curves (low uptake curves) and care should be taken to administer sufficient activity in clinical HRRT studies.

In addition to the 3D-FBP outlier above, there was another subject (subject \times) who showed consistently higher parameter values for reference tissue analyses applied to HR+ reconstructions. For example, RLogan DVR values for this particular subject were higher for HR+ (6.1 ± 2.5) than were normal values for either HR+ 2D-FBP + FORE (4.3 ± 1.6) or HRRT (4.0 ± 1.4). This subject showed a slightly lower SUV tail (last 3 time frames; 0.16) than did other subjects scanned on the HR+ (0.30 ± 0.09). However, noise-equivalent count rates were not lower for this particular subject ($2.97 \cdot 10^7$) than for the other subjects ($3.27 \cdot 10^7 \pm 0.5 \cdot 10^7$). In addition, random fractions were not higher for this particular subject (9.5% vs. $8.8\% \pm 1.6\%$ for the others). Therefore, the reason for the abnormal reference tissue parameters remains unknown.

After resolution matching, the reference tissue models showed lower HRRT parameter values than HR+ values (Fig. 3; Tables 4 and 5). This might be due to some bias in the HRRT reconstructions. In particular, reference tissue tracer concentrations are low (no specific binding) and are, therefore, more prone to bias (e.g., because of imperfections in the attenuation correction (15), scatter correction (11,34), or reconstruction (11,20,21,23,24) algorithms). Attenuation and scatter correction might also explain the somewhat poorer test-retest values for structures close to the skull, such as the frontal and temporal lobes. In addition, 2D simulations have shown that gap-filling strategies for the HRRT could cause a small negative bias in WM regions (such as pons) for 3D-FBP reconstructions (20). Furthermore, bias in HRRT 3D-FBP reconstructions might occur in cold regions when the contrast between background and cold region becomes too large (21).

However, as can be seen in Figures 2C and 2D and Tables 6 and 7, for most subjects a good correlation of DVR and BP_{ND} values was observed. Thus, the present study illustrates that higher values of kinetic reference tissue modeling data can be obtained using the HRRT as a result of the higher resolution (Tables 6 and 7), which is consistent with the findings of Leroy et al. (3).

Additional Remarks

Future improvements in (small) residual differences between the HR+ and the HRRT scanners can be expected when systematic bias, currently observed in short-duration

HRRT frames for 3D iterative reconstruction algorithms (11,21,23,24), can be removed (e.g., using iterative reconstruction algorithms that allow for negative image values, such as the NEG-ML algorithm) (35). In addition, new attenuation-correction strategies that show less overestimation of the size of the skull and a fully 3D iterative scatter-correction algorithm might improve the quantitative accuracy of reference tissue models for the HRRT, because reference regions generally have a lower uptake and are, therefore, more sensitive for (small) inaccuracies in scatter corrections.

CONCLUSION

Higher parameter values were obtained with the HRRT than with the HR+ scanner using either plasma input or reference tissue models. However, the outcome of reference tissue model analysis may be affected by low counts in the reference region causing bias in reconstruction methods of the HRRT or by inaccuracies in the attenuation and scatter corrections. The improvement of these methods is currently one of the primary goals of the HRRT community. However, the higher pharmacokinetic parameter values observed in most subjects are primarily a result of the higher resolution of the HRRT, as differences of the HRRT, compared with HR+, disappear after resolution matching. Therefore, this study provides further evidence that the HRRT can be used for quantitative studies with a higher spatial resolution in a clinical setting.

ACKNOWLEDGMENTS

We thank Jurgen E.M. Mourik for his useful comments and suggestions; Nelleke Tolboom, Saskia P.A. Wolfensberger, and Jochem P. Bremmer for their assistance in acquiring subject data; the technology staff of the Department of Radiology for the acquisition of the MRI data; and the radiochemistry and technology staff of the Department of Nuclear Medicine & PET Research for the production of isotopes and acquisition of PET data. This work was financially supported by the Netherlands Organization for Scientific Research (NWO), VIDI grant 016.066.309.

REFERENCES

1. de Jong HWAM, van Velden FHP, Kloet RW, Buijs FL, Boellaard R, Lammertsma AA. Performance evaluation of the ECAT HRRT: an LSO-LYSO double layer high resolution, high sensitivity scanner. *Phys Med Biol.* 2007;52:1505–1526.
2. Wienhard K, Schmand M, Casey ME, et al. The ECAT HRRT: performance and first clinical application of the new high resolution research tomograph. *IEEE Trans Nucl Sci.* 2002;49:104–110.
3. Leroy C, Comtat C, Trebossen R, Syrota A, Martinot JL, Ribeiro MJ. Assessment of ^{11}C -PE2I binding to the neuronal dopamine transporter in humans with the high-spatial-resolution PET scanner HRRT. *J Nucl Med.* 2007;48:538–546.
4. Heiss WD, Habedank B, Klein JC, et al. Metabolic rates in small brain nuclei determined by high-resolution PET. *J Nucl Med.* 2004;45:1811–1815.
5. Ginovart N, Willeit M, Rusjan P, et al. Positron emission tomography quantification of [^{11}C]-(+)-PHNO binding in the human brain. *J Cereb Blood Flow Metab.* 2007;27:857–871.

6. Willeit M, Ginovart N, Graff A, et al. First human evidence of D-amphetamine induced displacement of a D2/3 agonist radioligand: a [¹¹C]-(+)-PHNO positron emission tomography study. *Neuropsychopharmacology*. 2008;33:279–289.
7. Hirvonen J, Johansson J, Teras M, et al. Measurement of striatal and extrastriatal dopamine transporter binding with high-resolution PET and [¹¹C]PE2I: quantitative modeling and test-retest reproducibility. *J Cereb Blood Flow Metab*. 2008;28:1059–1069.
8. Boellaard R, van Lingen A, Lammertsma AA. Experimental and clinical evaluation of iterative reconstruction (OSEM) in dynamic PET: quantitative characteristics and effects on kinetic modeling. *J Nucl Med*. 2001;42:808–817.
9. Brix G, Zaers J, Adam LE, et al. Performance evaluation of a whole-body PET scanner using the NEMA protocol. National Electrical Manufacturers Association. *J Nucl Med*. 1997;38:1614–1623.
10. Adam LE, Zaers J, Ostertag H, Trojan H, Bellemann ME, Brix G. Performance evaluation of the whole-body PET scanner ECAT EXACT HR+ following the IEC standard. *IEEE Trans Nucl Sci*. 1997;44:1172–1179.
11. van Velden FHP, Kloet RW, de Jong HWAM, Lammertsma AA, Boellaard R. Quantitative experimental comparison of HRRT versus HR+ PET brain studies. *IEEE Nucl Sci Symp Conf Rec*. 2006;5:3097–3099.
12. Sossi V, de Jong HWAM, Barker WC, et al. The second generation HRRT: a multi-centre scanner performance investigation. *IEEE Nucl Sci Symp Conf Rec*. 2005;4:2195–2199.
13. Knoess C, Rist J, Michel C, et al. Evaluation of single photon transmission for the HRRT. *IEEE Nucl Sci Symp Conf Rec*. 2003;3:1936–1940.
14. Eriksson L, Wienhard K, Eriksson M, et al. NEMA count-rate evaluation of the first and second generation of the Ecac Exact and Ecac Exact HR family of scanners. *IEEE Trans Nucl Sci*. 2002;49:640–643.
15. van Velden FHP, Kloet RW, van Berckel BNM, et al. Impact of attenuation correction strategies on the quantification of high resolution research tomograph PET studies. *Phys Med Biol*. 2008;53:99–118.
16. Boellaard R, van Lingen A, van Balen SC, Hoving BG, Lammertsma AA. Characteristics of a new fully programmable blood sampling device for monitoring blood radioactivity during PET. *Eur J Nucl Med*. 2001;28:81–89.
17. Lubberink M, Boellaard R, Greuter HNJM, Lammertsma AA. Effect of uncertainty in plasma metabolite levels on kinetic analysis of [¹¹C] flumazenil and [¹¹C] (R)-PK11195 PET studies [abstract]. *Neuroimage*. 2004;22(suppl 2):T119–T120.
18. van Rij CM, Huitema ADR, Swart EL, et al. Population plasma pharmacokinetics of C-11-flumazenil at tracer concentrations. *Br J Clin Pharmacol*. 2005; 60:477–485.
19. Salmi E, Aalto S, Hirvonen J, et al. Measurement of GABAA receptor binding in vivo with [¹¹C]flumazenil: a test-retest study in healthy subjects. *Neuroimage*. 2008;41:260–269.
20. van Velden FHP, Kloet RW, van Berckel BNM, Molthoff CFM, Lammertsma AA, Boellaard R. Gap filling strategies for 3-D-FBP reconstructions of high-resolution research tomograph scans. *IEEE Trans Med Imaging*. 2008;27:934–942.
21. van Velden FHP, Kloet RW, van Berckel BNM, Lammertsma AA, Boellaard R. Accuracy of 3-dimensional reconstruction algorithms for the high-resolution research tomograph. *J Nucl Med*. 2009;50:72–80.
22. Strother SC, Casey ME, Hoffman EJ. Measuring PET scanner sensitivity: relating count rates to image signal-to-noise ratios using noise equivalent counts. *IEEE Trans Nucl Sci*. 1990;37:783–788.
23. Johansson J, Oikonen V, Teras M, van Berckel BNM, Lammertsma AA, Boellaard R. Comparison of 3D-OP-OSEM and 3D-FBP reconstruction algorithms for high-resolution research tomograph studies: effects of randoms estimation methods. *Phys Med Biol*. 2008;53:3217–3230.
24. Johansson J, Oikonen V, Teras M. Quantitative brain imaging using the new, fast iterative histogram-mode reconstruction for the HRRT PET scanner. *IEEE Nucl Sci Symp Conf Rec*. 2007;5:3463–3467.
25. Byars LG, Sibomana M, Burbar Z, et al. Variance reduction on randoms for delayed coincidence histograms for the HRRT. *IEEE Nucl Sci Symp Conf Rec*. 2005;5:2622–2626.
26. Boellaard R, Lubberink M, de Jong HWAM, Kropholler M, Lammertsma AA. Application of various iterative reconstruction methods for quantitative 3D dynamic brain PET studies. *IEEE Nucl Sci Symp Conf Rec*. 2004;4:2553–2556.
27. Logan J. Graphical analysis of PET data applied to reversible and irreversible tracers. *Nucl Med Biol*. 2000;27:661–670.
28. Boellaard R, Knaapen P, Rijbroek A, Luurtsema GJ, Lammertsma AA. Evaluation of basis function and linear least squares methods for generating parametric blood flow images using ¹⁵O-water and positron emission tomography. *Mol Imaging Biol*. 2005;7:273–285.
29. Logan J, Fowler JS, Volkow ND, Wang GJ, Ding YS, Alexoff DL. Distribution volume ratios without blood sampling from graphical analysis of PET data. *J Cereb Blood Flow Metab*. 1996;16:834–840.
30. Gunn RN, Lammertsma AA, Hume SP, Cunningham VJ. Parametric imaging of ligand-receptor binding in PET using a simplified reference region model. *Neuroimage*. 1997;6:279–287.
31. Lammertsma AA, Hume SP. Simplified reference tissue model for PET receptor studies. *Neuroimage*. 1996;4:153–158.
32. Boellaard R, Yaqub M, Lubberink M, Lammertsma AA. PPET: a software tool for kinetic and parametric analysis of dynamic PET studies [abstract]. *Neuroimage*. 2006;31(suppl 2):T62.
33. Slifstein M, Laruelle M. Effects of statistical noise on graphic analysis of PET neuroreceptor studies. *J Nucl Med*. 2000;41:2083–2088.
34. Mourik JEM, van Velden FHP, Lubberink M, et al. Image derived input functions for dynamic high resolution research tomograph PET brain studies. *Neuroimage*. 2008;43:676–686.
35. Nuyts J, Stroobants S, Dupont P, Vleugels S, Flamen P, Mortelmans L. Reducing loss of image quality because of the attenuation artifact in uncorrected PET whole-body images. *J Nucl Med*. 2002;43:1054–1062.